Scripta Materialia 180 (2020) 6–10

Contents lists available at ScienceDirect

Scripta Materialia

journal homepage: www.elsevier.com/locate/scriptamat

Temperature threshold for preferential bubble formation on grain boundaries in tungsten under *in-situ* helium irradiation

O. El-Atwani[a,*], W.S. Cunningham[b], D. Perez[c], E. Martinez[c], J.R. Trelewicz[b,d], M. Li[e], S.A. Maloy[a]

[a] Materials Science and Technology Division, Los Alamos National Laboratory, Los Alamos, NM, United States
[b] Department of Materials Science and Chemical Engineering, Stony Brook University, Stony Brook, NY, United States
[c] Theoretical Division, Los Alamos National Laboratory, Los Alamos, NM, United States
[d] Institute for Advanced Computational Science, Stony Brook University, Stony Brook, NY, United States
[e] Division of Nuclear Engineering, Argonne National Laboratory, Argonne, IL, United States

ARTICLE INFO

Article history:
Received 7 November 2019
Revised 9 January 2020
Accepted 11 January 2020

Keywords:
Grain boundaries
Implantation
In-situ
Helium-vacancy complexes
Electron microscopy

ABSTRACT

Understanding a material's radiation tolerance requires examining its performance under different irradiation conditions. Here, we investigate the radiation tolerance in terms of helium bubble damage in tungsten irradiated *in-situ* with 16 keV helium at 1073 K and 1223 K. Damage evolution represented by helium bubble density, size and total change in volume in the grain matrices and the grain boundaries are quantified as a function of fluence. Preferential large bubble formation and a higher change in volume on the grain boundaries occurred at 1223 K, suggesting faster migration of certain helium-vacancy complexes as confirmed by a diffusion-reaction model.

Published by Elsevier Ltd on behalf of Acta Materialia Inc.

Plasma facing and divertor materials in fusion devices have to withstand severe environments of fast neutrons, particles fluxes, thermal loads (5–20 MW/m^2), and transient thermal loads [1]. Neutron irradiation produces solid transmutation products (rhenium, osmium, among others) and substantial helium gas [2]. Helium (He) concentrations due to transmutation can reach levels of about 2000 appm for the anticipated 5 year lifetime of a plasma facing component, which corresponds to damage levels of ~200 dpa [1]. The transmuted He can enhance cavity formation via stabilizing vacancies [3,4] and can also reach grain boundaries (either via interstitial helium diffusion or after the formation of helium-vacancy complexes), in turn promoting the formation of grain boundary bubbles [5]. Bubble formation on the grain boundaries can be exacerbated in nanocrystalline material candidates due to the shorter effective diffusion lengths of He or He associated defects to the grain boundaries as demonstrated by El Atwani et al. on ultrafine and nanocrystalline (NC) pure tungsten irradiated with low energy He [6,7]. The mechanisms governing bubble formation and their resulting shape, concentration, and pressures are not yet fully understood, but have exhibited a range of different behavior that depends on the irradiation conditions. Recent literature has demonstrated that bubbles might serve as dislocation sources and shearable obstacles in single crystalline copper [8], which are rationalized to enhance the mechanical properties of NC materials when neglecting the effect of possible grain boundary bubbles and the shape and concentration of He in the bubbles. A study by Cunningham et al. [9] has shown a decrease in hardness (softening) in ultrafine-grained tungsten (Fig. 6) containing bubble-loaded grain boundaries under certain He implantation conditions, which transitioned to faceted cavities at higher irradiation temperatures. Therefore, it is critical to understand how He bubble size and distribution change with irradiation parameters and its consequences for the performance of tungsten as a plasma facing material. Temperature has been demonstrated to be an important factor influencing cavity size and shape with preferential formation on grain boundaries occurring at temperatures exceeding the helium-vacancy migration thresholds [10]. However, the distributions of cavities on grain boundaries and grain matrices, the temperature threshold for preferential cavity formation, helium trapping efficiency as a function of temperature, and the mechanism by which these large cavities are formed on the grain boundaries, remain to be elucidated.

Here, we study via *in-situ* irradiation/transmission electron microscopy (TEM), low energy (16 keV) helium implantation effects on tungsten (a plasma facing material and divertor candidate

* Corresponding author.
E-mail address: oelatwan25@gmail.com (O. El-Atwani).

https://doi.org/10.1016/j.scriptamat.2020.01.013
1359-6462/Published by Elsevier Ltd on behalf of Acta Materialia Inc.

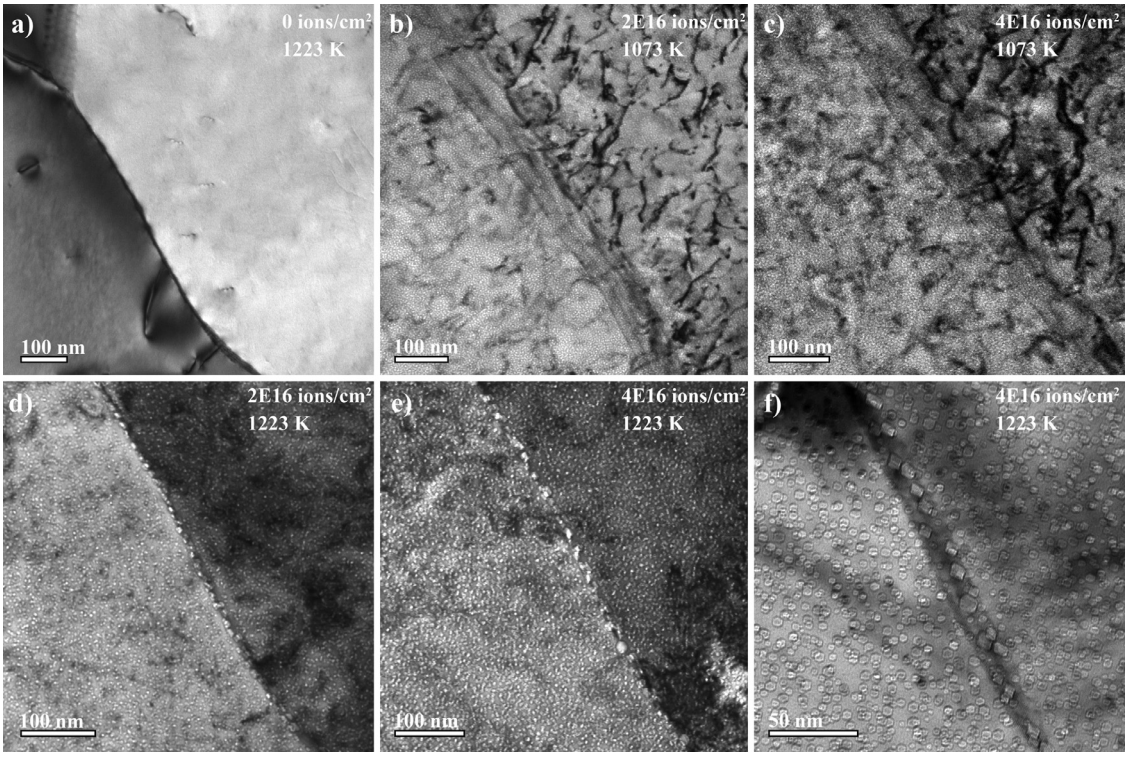

Fig. 1. Bright-field in-situ TEM micrographs of a) pristine tungsten sample, (b) and (c) 16 KeV He^+ implanted tungsten to 2×10^{16} cm^{-2} and 4×10^{16} cm^{-2} at 1073 K respectively, (d) and (e) 16 KeV He^+ implanted tungsten to 2×10^{16} cm^{-2} and 4×10^{16} cm^{-2} at 1223 K respectively, and (f) higher magnification micrograph of the 1223 K implanted tungsten demonstrating facetted cavity formation.

for fusion power due to its attractive physical properties) at two elevated temperatures of 1073 and 1223 K. The experiments were performed using the Intermediate Voltage Electron Microscope (IVEM) attached to an ion accelerator at Argonne National Laboratory. Irradiations employed 16 keV He ions of 1×10^{13} $cm^{-2} \bullet s^{-1}$ flux on tungsten (ESPI metals, USA) thin foils approximately 100 nm thick prepared by electropolishing with a 0.5% NaOH solution. Details about the microstructure of an ESPI tungsten sample are presented elsewhere [11]. Using the Kinchin-Pease model in the Stopping Range of Ions in Matter (SRIM) Monte Carlo computer code (version 2013) [12] where 70 eV [13] was taken as the displacement threshold, the He depth peak (Figure S1 in the supplemental) aligned with the center of the foils. While 16 keV is a low energy implantation compared to energies expected from transmutation reactions, implantation energies are restricted to foil thicknesses during in-situ TEM experiments, and the work can still describe bubble formation and growth behavior under implantation conditions where atomic displacements can occur. The experiments (with *in-situ* TEM imaging) were performed for ~ 4000 s corresponding to a total fluence of 4×10^{16} cm^{-2} or ~ 6.3% He implantation in tungsten. Bubble growth within the grain matrix and the adjacent grain boundary was examined with bubble size and density quantified as a function of time for the two different temperatures. Quantification methods similar to Ref. [14] were used. The difference in the total amount of He bubbles in the grain boundaries as a function of temperature was explained in the context of a diffusion-reaction model [15,16]. In particular, a single species model was used to compute the integrated flux to grain boundaries in a 1 μm grain as a function of the migration energy (ΔE_m) and the pre-factor (ν). The diffusivity was calculated following harmonic transition state theory as $D = a^2 \nu \exp(\Delta E_m / k_B T)$, where a is the lattice parameter.

A magnified view of a pristine grain boundary in the tungsten samples is shown in Fig. 1a and followed by irradiation at 1073 and 1223 K in Fig. 1(b-f). The defect microstructure formed under the different irradiation conditions exhibited a number of differences. The microstructure of the sample irradiated at 1073 K exhibited spherically shaped bubbles distributed uniformly between the matrix and grain boundary. Conversely, the sample irradiated at 1223 K demonstrated preferential formation of bubbles on the grain boundaries, which grew faster than those in the matrix as a function of fluence (Figures d & e). At the highest fluence, the larger bubbles occupying the grain boundaries were generally faceted in nature as observed in Fig. 1f and is consistent with other studies on He bubble formation on grain boundaries in tungsten [7,14]. The quantification of the bubble density and average area (delineated for the grain matrix and boundary) as well as total change in volume percentage of the matrix material found using $\frac{\Delta v}{v} = \frac{4}{3}\pi r_c^3 N_v$ where N_v is the bubble density in a 100 nm thick foils and r_c is the radius of the bubble, are shown at both temperatures in Fig. 2 as a function of fluence (three data points for the 1073 K sample and 36 data points for the 1233 K sample). At 1073 K, the density of the bubbles was independent of fluence while the average bubble area increased (Fig. 2a) with increasing fluence. Bubbles on the grain boundaries exhibited a similar area to those in the grain matrices (Fig. 2c). At 1223 K, however, while the density saturated in Fig. 2b to a value ~ 63% lower than the 1073 K case, the average bubble area continued to increase in the grain matrices (68% more than the 1073 K case). The scaling of bubble size in the grain boundaries at 1223 K was noticeably different with the average area increasing exponentially up to the maximum dose in Fig. 2d. The average change in volume due to bubble formation in the grain matrices at 1073 K was about 2% compared to ~1.7% at 1223 K. All values for the grain matrices at both temperatures are listed in Table 1.

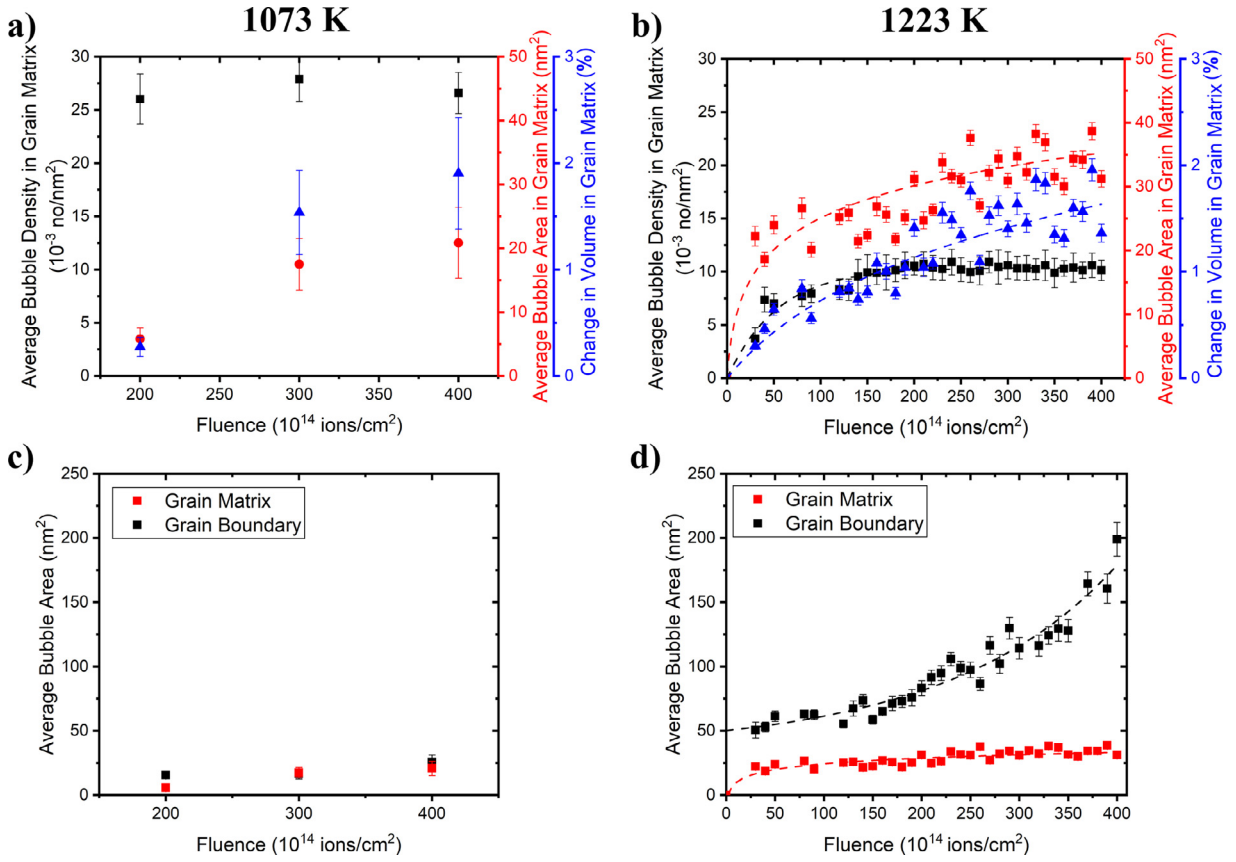

Fig. 2. (a) and (b), Bubble density, size, and total change in volume pecentage due to bubble formation in the grain matrices at 1073 K and 1223 K, respectively, as a function of fluence. The lines are a guide for the eye only. (c) and (d) Average bubble size in the grain matrices and the grain boundaries at 1073 and 1223 K, respectively, as a function of fluence. (For interpretation of the references to color in this figure legend, the reader is referred to the web version of this article.)

Table 1
Bubble density, average area and total change in volume in the grain matrices at 1073 and 1223 K.

	Bubble matrix								
	Bubble density (no/nm^2)			Bubble area (nm^2)			Change in volume		
Fluence (ions/cm^2)\Temperature(K)	1073	1223	1223/1073	1073	1223	1223/1073	1073 (%)	1223 (%)	1223/1073
2.00E+16	0.026 ±0.003	0.010 ±0.002	0.385 ±0.110	5.807 ±1.731	28.553 ±7.465	4.917 ±1.824	0.274 ±0.089	1.161 ±0.390	4.239 ±1.671
3.00E+16	0.028 ±0.003	0.010 ±0.002	0.370 ±0.083	17.499 ±4.054	31.472 ±8.862	1.798 ±0.681	1.537 ±0.395	1.372 ±0.509	0.893 ±0.424
4.00E+16	0.027 ±0.002	0.010 ±0.001	0.390 ±0.062	20.856 ±5.543	33.553 ±9.222	1.609 ±0.662	1.905 ±0.525	1.515 ±0.528	0.795 ±0.392

The differences in average bubble area and shape on grain boundaries between 1073 and 1223 K cases can be related to differences in defect fluxes to the grain boundaries and/or defect migration on the grain boundaries themselves. To understand these differences, bubble density and total change in volume on the grain boundaries at both temperatures were quantified using inclined grain boundaries. The ratio of the bubble density, average area, and change in volume on the grain boundaries and the grain matrices for similar fluences at both temperatures are plotted in Fig. 3. All values for bubbles occupying the grain boundaries at both temperatures are reported in Table 2.

At 1223 K, bubbles in the grain matrices and grain boundaries generally exhibited a smaller density but larger area (except for the low fluence of 2×10^{16} cm^{-2} where bubble sizes are the same) relative to the 1073 K case. The total change in volume percentage in the grain matrices was higher at 2×10^{16} cm^{-2} then decreased with fluence to effectively produce a similar change in volume to the 1073 K case. The total change in volume on the grain boundaries followed the opposite trend, approaching 4 times the 1073 K case at the maximum fluence of 4×10^{16} cm^{-2}. These findings substantiate several phenomena: (1) grain boundaries are He trapping sites (2D trapping nature vs 3D trapping within the grain matrices) [17], (2) defect fluxes to the grain boundaries at the two temperatures are different, (3) migration of certain defects (e.g. vacancies or some He-vacancy complexes) at 1223 K on the grain boundaries is sufficiently high to facilitate the formation of larger, faceted bubbles, and (4) there is a temperature threshold for preferential faceted bubble formation and enhanced He trapping efficiency. The latter is a particularly important parameter since it has been demonstrated that ultrafine tungsten with large bubble-loaded grain boundaries after low energy He implantation suffers from mechanical property degradation manifested by a reduced hardness relative to pristine tungsten during nanoindentation [9].

The fundamental mechanisms leading to bubble formation on the grain boundaries can involve a number of defect transport

Table 2
Bubble density, average area and total change in volume percentages in the grain boundaries at 1073 and 1223 K.

	Grain boundary								
	Bubble density (no/nm^2)			Bubble area (nm^2)			Change in volume		
Fluence (ions/cm^2)\Temperature (K)	1073	1223	1223/1073	1073	1223	1223/1073	1073 (%)	1223 (%)	1223/1073
2.00E+16	0.021 ±0.001	0.0035 ±0.0009	0.166 ±0.044	15.463 ±4.390	61.003 ±8.604	3.945 ±1.251	0.963 ±0.277	1.255 ±0.370	1.303 ±0.537
3.00E+16	0.020 ±0.001	0.0038 ±0.0010	0.191 ±0.053	16.584 ±4.725	103.186 ±22.258	6.222 ±2.223	1.015 ±0.294	3.012 ±1.045	2.967 ±1.041
4.00E+16	0.017 ±0.001	0.0033 ±0.0009	0.193 ±0.053	25.680 ±8.874	204.732 ±59.522	7.972 ±3.600	1.698 ±0.602	7.365 ±2.877	4.337 ±1.288

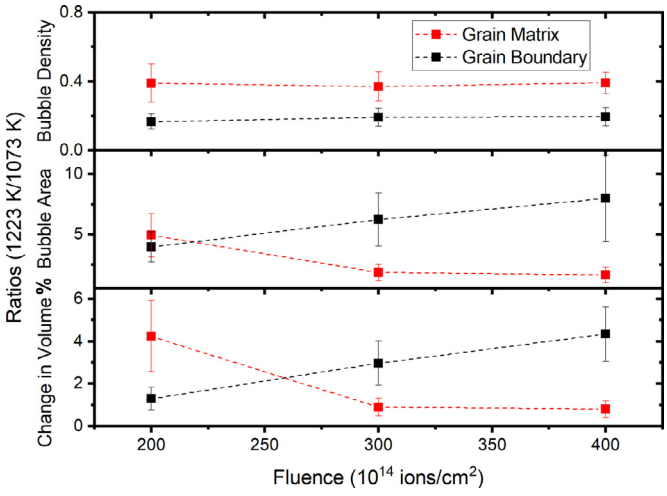

Fig. 3. Average bubble density, area, and total change in volume percentage for 1223 K/1073 K in the grain matrices and the grain boundaries as a function of fluence. (For interpretation of the references to color in this figure legend, the reader is referred to the web version of this article.)

processes: (1) diffusion of He interstitials to the grain boundaries, coalescence, and trap mutation, (2) vacancy migration to grain boundaries and binding to previously trapped He interstitials, and (3) He-vacancy complex migration to grain boundaries, coalescence, and trap mutation. By comparing the results between the two different temperatures, we can provide insights into the mechanisms governing preferential bubble formation and growth within the grain boundaries at 1223 K in the subjected tungsten samples. Migration of He interstitials in tungsten has an activation energy of ~ 0.06 eV [18]; it is therefore expected that He migration will transpire at both temperatures, which indicates that increased He interstitial transport is not the leading cause of the rapid bubble growth in the grain boundaries at 1223 K. Both vacancies and several He-vacancy complexes can migrate at both irradiation temperatures. However, depending on the migration energies and pre-factors, the total integrated flux of some of these defects can be significantly higher at 1223 K.

To understand the origin of the volume change due to grain boundary bubble formations, we analyzed the defect flux to the grain boundaries at both temperatures using a 1-D reaction-diffusion equation. A domain size of 1 μm and mesh size of 2 nm were employed with a source of particles of 0.002 dpa/s (similar to experiments) introduced for 4000 s (note that not all simulations reached steady-state). The diffusivity of the moving species was varied by modifying the migration energy and pre-factor. The total integrated flux at the boundary was computed for both temperatures with the ratio of the two fluxes plotted as a contour map in Fig. 4 as a function of the migration barrier and pre-factor. Assuming that the experimental change in volume (4.3 times larger at 1223 K with respect to 1073 K with an error bar of ± 1.28) at the grain boundaries is due to the difference in the number of particles (particle flux) that reach the boundary from the matrix, the combination of migration energy and pre-factor of the responsible defect should fall around the yellow area (from green to the light red) in Fig. 4. We also note that differences in the grain boundary character on change in volume is not expected to shift the change in volume value outside the green region.

Given vacancy migration energy in tungsten of ~ 1.7 eV [19] and typical pre-factors for vacancy diffusion on the order of 10^{12} s^{-1}, the second route for bubble formation appears unlikely as the combination of these values falls in the dark blue region in Fig. 4. In addition, the pre-factor for vacancy clusters was shown to linearly (high slope) decrease for large clusters [20], and thus, the pre-factor for He-vacancy complexes should be lower than the 10^{12} s^{-1}. The green to light red area has migration energies that fit He-vacancy complexes with vacancy to He ratios greater than 1. For 16 keV He ions, nearly 7 vacancies will be created for every He ion. While some of these vacancies can recombine with interstitials, other vacancies can rapidly form He-V complexes; in this case, a ratio of vacancy/He greater than 1 is expected. Using density functional theory (DFT) calculations, the migration energy of He-V_2 complexes has been shown to be 2.04 eV [21]. In addition, while the grain boundaries at 1223 K exhibited a 4.3X increase in the volume change at the grain boundaries, the volume change in the grain matrix did not decrease by the same ratio. Some He-vacancy complexes might not have clustered, due to lower mobility in the same way (as in the 1223 K case) at 1073 K and therefore, did not reach a sufficient size to be resolved by TEM. This implies that the change in volume ratio in both the grain matrices and grain boundaries should be smaller than the reported values. However, due to the high density of bubbles and thus, low diffusion length for these clusters, this change is not expected to be large. A smaller value of the change in volume at the grain boundaries would shift the migration energy area in Fig. 4 to lower values (e.g., within the green region), which is more consistent with the reported data for He-vacancy complexes with vacancy/He ratios greater than 1. Finally, defect annihilation and recombination are different at both temperatures and expected to be higher in the grain matrices at 1223 K, which in turn can explain the low ratio for the change in volume in the grain matrices.

These results indicate that a temperature threshold for preferential bubble formation on the grain boundaries should exist but can vary depending on the implantation conditions (e.g. implantation energy which can dictate the He/vacancy ratio) and the implanted material due to differences in migration energies and pre-exponential factors of He-vacancy complexes diffusion equation. This can set a safety window for the operation of materials which will be exposed to helium implantations or large amount of helium due to transmutation reactions since large facetted bubbles on grain boundaries can lead to mechanical softening demonstrated via nanoindentation experiments on He implanted tungsten [9]. Further mechanical property studies on the different nuclear mate-

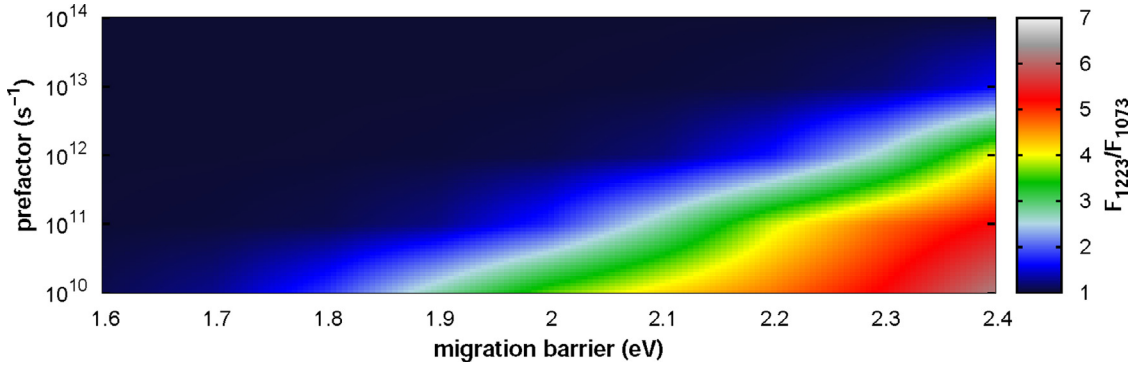

Fig. 4. Defect flux ratio at 1223 K/ 1073 K as a function of a pre-factor term and migration barrier for an Arrhenius type equation as determined from the diffusion reaction model. (For interpretation of the references to color in this figure legend, the reader is referred to the web version of this article.)

rials' candidates with high grain boundary density (e.g. nanocrystalline materials) below and above the temperature threshold for preferential and large bubble formation on grain boundaries are essential for understanding their mechanical behavior and the safe temperature windows for reactor operation. The results in this work were acquired using *in-situ* implantations on thin foil samples which are susceptible to surface proximity effects [22]. Surfaces can act as sinks and due to the rapid interstitial migration and He-vacancy complex formation, a percentage of interstitials can be annihilated at the surfaces. However, this effect would be similar at both temperatures due to the low migration energy of interstitials in tungsten (0.054 eV) [23] and therefore, the damage trends and the relative damage comparison at both temperatures are valid. In addition, the high interstitial damage observed in the samples at some diffraction conditions (e.g. Fig. 1c) demonstrates that surface proximity effects did not dominate the results.

In summary, He ion implantation was performed *in-situ* in the TEM on tungsten at 1073 K and 1223 K. Grain boundaries at 1223 K were shown to exhibit preferential bubble formation with larger bubbles as compared with the grain matrices. Enhanced He trapping and bubble formation (with smaller densities) at 1223 K relative to 1073 K suggested a temperature threshold for He-vacancy migration and trapping at energies similar to this study. Reaction-diffusion calculations suggest that migration of the He-vacancy complex (of vacancy/He ratio greater than 1) and rapid coalescence at the grain boundaries at 1223 K constitute the responsible mechanism for such preferential trapping and large faceted bubble formation in the grain boundaries.

Declaration of Competing Interest

The authors declare that they have no competing interests.

Acknowledgements

This work was supported by the U.S. Department of Energy, Office of Nuclear Energy under DOE Idaho Operations Office Contract DE-AC07- 051D14517 as part of a Nuclear Science User Facilities experiment. Research presented in this article was also supported by the Laboratory Directed Research and Development program of Los Alamos National Laboratory under project number 20160674PRD3. WSC and JRT acknowledge support for this work from the National Science Foundation through Grant 1810040. We gratefully acknowledge the support of the U.S. Department of Energy through the LANL/LDRD Program and the G. T. Seaborg Institute for this work. DP and EM acknowledge support by the U.S. Department of Energy, Office of Science, Office of Fusion Energy Sciences, and Office of Advanced Scientific Computing Research through the Scientific Discovery through Advanced Computing (SciDAC) project on Plasma–Surface Interactions under Award No. DE-SC0008875.

Supplementary materials

Supplementary material associated with this article can be found, in the online version, at doi:10.1016/j.scriptamat.2020.01.013.

References

[1] S.J. Zinkle, L.L. Snead, Ann. Rev. Mater. Res. 44 (2014) 241–267.
[2] Y. Katoh, L.L. Snead, L.M. Garrison, X. Hu, T. Koyanagi, C.M. Parish, P.D. Edmondson, M. Fukuda, T. Hwang, T. Tanaka, A. Hasegawa, J. Nucl. Mater. 520 (2019) 193.
[3] D. Reed, Radiat. EIT 31 (3) (1977) 129–147.
[4] C. Becquart, C. Domain, J. Nucl. Mater. 385 (2) (2009) 223–227.
[5] P. Lane, P. Goodhew, Philos. Mag. A 48 (6) (1983) 965–986.
[6] O. El-Atwani, J.A. Hinks, G. Greaves, J.P. Allain, S.A. Maloy, Mater. Res. Lett. 5 (5) (2017) 343–349.
[7] O. El-Atwani, J.A. Hinks, G. Greaves, S. Gonderman, T. Qiu, M. Efe, J.P. Allain, Sci. Rep. 4 (2014) 4716.
[8] M.-.S. Ding, J.-.P. Du, L. Wan, S. Ogata, L. Tian, E. Ma, W.-.Z. Han, J. Li, Z.-.W. Shan, Nano Lett. 16 (7) (2016) 4118–4124.
[9] W.S. Cunningham, J.M. Gentile, O. El-Atwani, C.N. Taylor, M. Efe, S.A. Maloy, J.R. Trelewicz, Sci. Rep. 8 (1) (2018) 2897.
[10] O. El-Atwani, K. Hattar, J. Hinks, G. Greaves, S. Harilal, A. Hassanein, J. Nucl. Mater. 458 (2015) 216–223.
[11] O. El-Atwani, E. Esquivel, M. Efe, E. Aydogan, Y. Wang, E. Martinez, S. Maloy, Acta Mater. 149 (2018) 206–219.
[12] J.F. Ziegler, M.D. Ziegler, J.P. Biersack, Beam Interact. Mater. Atoms 268(11) (2010) 1818–1823.
[13] A.E.-. e1, Standard Practice for Neutron Radiation Damage Simulation By Charged Particle Radiation, American society of Testing and Material Wes Conshohocken, PA, 2009.
[14] O. El-Atwani, J. Nathaniel, A. Leff, B. Muntifering, J. Baldwin, K. Hattar, M. Taheri, J. Nucl. Mater. 484 (2017) 236–244.
[15] S.I. Golubov, A. Barashev, R.E. Stoller, Compr. Nucl. Mater. 1 (2012) 357–391.
[16] A.Y. Dunn, L. Capolungo, E. Martinez, M. Cherkaoui, J. Nucl. Mater. 443 (1–3) (2013) 128–139.
[17] B.N. Singh, A.J.E. Foreman, Philos. Mag. 29 (4) (1974) 847–858.
[18] C.S. Becquart, C. Domain, Phys. Rev. Lett. 97 (19) (2006) 196402.
[19] R.W. Balluffi, J. Nucl. Mater. 69 (1978) 240–263.
[20] N. Castin, A. Bakaev, G. Bonny, A. Sand, L. Malerba, D. Terentyev, J. Nucl. Mater. 493 (2017) 280–293.
[21] C. González, R. Iglesias, JMatS 49 (23) (2014) 8127–8139.
[22] M. Li, M. Kirk, P. Baldo, D. Xu, B. Wirth, Philos. Mag. 92 (16) (2012) 2048–2078.
[23] F. Dausinger, H. Schultz, Phys. Rev. Lett. 35 (26) (1975) 1773.